PHYSICAL REVIEW B **84**, 014306 (2011)

Vibrational dynamics of the filled skutterudites $M_{1-x}Fe_4Sb_{12}$ (M = Ca, Sr, Ba, and Yb): Temperature response, dispersion relation, and material properties

Michael Marek Koza,[1,2] Andreas Leithe-Jasper,[2] Helge Rosner,[2] Walter Schnelle,[2] Hannu Mutka,[1] Mark Robert Johnson,[1] Michael Krisch,[3] Lucia Capogna,[1,4] and Yuri Grin[2]

[1] *Institut Laue Langevin, 6 Rue Jules Horowitz, B.P. 156, F-38042 Grenoble, Cedex 9, France*
[2] *Max–Planck–Institut für Chemische Physik fester Stoffe, Nöthnitzer Straße 40, D-01187 Dresden, Germany*
[3] *European Synchrotron Radiation Facility, 6 Rue Jules Horowitz, B.P. 220, F-38043 Grenoble, Cedex 9, France*
[4] *OGG IOM CNR Grenoble, 6 Rue Jules Horowitz, F-38042 Grenoble, Cedex 9, France*

(Received 12 July 2010; revised manuscript received 20 October 2010; published 27 July 2011)

The vibrational dynamics of the ternary $Ca_{1-x}Fe_4Sb_{12}$, $Ba_{1-x}Fe_4Sb_{12}$, $Sr_{1-x}Fe_4Sb_{12}$, and $Yb_{1-x}Fe_4Sb_{12}$ compounds is studied for its temperature dependence, dispersion relations, and material properties by experiments and *ab initio* powder-averaged lattice-dynamics (PALD) calculations. The experimental techniques used are high-resolution inelastic neutron scattering (INS) and inelastic x-ray scattering (IXS). Vibrational properties of polycrystalline material have been mapped out in an extensive energy-momentum phase space facilitating the study of powder-averaged phonon-dispersion relations within the first and second Brillouin zones. Qualitatively, the experimental dynamic structure factor $S(Q,\omega)$ matches, to a high degree, PALD calculations allowing different schemes of collective vibrational eigenmodes to be evaluated. From the PALD calculations, quantitative values of velocity of sound, Debye temperatures, and elastic, bulk, and Young's moduli are computed. The variation of the generalized density of states $G(\omega)$ with temperature is studied experimentally in the range from 2 to 600 K. No particular anomalies in the collective dynamics are observed apart from a global softening of $G(\omega)$ upon heating.

DOI: 10.1103/PhysRevB.84.014306 PACS number(s): 63.20.dd, 63.20.Pw, 61.05.fg

I. INTRODUCTION

The observation that heat transport in ternary skutterudite compounds of type $Ce_{1-x}Fe_yCo_{4-y}Sb_{12}$ (space group $Im\bar{3}$) can be strongly reduced by altering the chemical compostion by $x \neq 0$ and $y \neq 0$ (Ref. 1) has attracted appreciable interest from the materials research community. A strongly reduced thermal conductivity is a prerequisite for semiconducting materials to achieve a high thermoelectric figure of merit.[2–4] Since electronic transport should be affected as weakly as possible, the reduction of the contribution of lattice vibrations to thermal conductivity is the focus of research activities. It is of interest to find, analyze, and reliably establish mechanisms for diminishing the propagation of the heat-carrying collective long-wavelength modes, i.e., acoustic phonons. The experimental study of acoustic phonons has to be performed with a quantitative mapping of the momentum-energy relationship, as only then properties such as phonon dispersion and form factors, phonon widths and, hence, phonon mean-free path and life time, anharmonicity effects and, thus, phonon-phonon and phonon-electron interactions become directly accessible.

In preceding publications (Refs. 5 and 6), we have addressed the microscopic dynamics of the ternary skutterudite compounds $M_{1-x}Fe_4Sb_{12}$ with M = Ca, Sr, Ba, La, Ce, and Yb and their corresponding microscopic observables monitored by different techniques. The core experimental work was based on high-resolution inelastic neutron scattering (INS), neutron diffraction, and specific-heat measurements. Experimentally obtained data were backed up by *ab initio* density-functional theory (DFT) lattice-dynamics calculations. Apart from structural parameters, observables were related to the phonon density of states $Z(\omega)$ of the compounds. The phonon density of states has been accessed in the INS experiments as a neutron-weighted generalized density of states $G(\omega)$. In brief, we have demonstrated that the dynamic properties of the so-called filled skutterudites can be well captured by the concept of harmonic crystals and that experimental data can be well matched by DFT lattice-dynamics results that are computed for $T = 0$ K.

Recent theoretical and molecular dynamics studies go beyond the harmonic-crystal model and investigate anharmonic effects as the possible origin of reduced thermal conductivity. The theoretical study of isotropic models by Dahm and Ueda[7] and Yamakage *et al.*[8] result in a pronounced and characteristic frequency shift of dispersive modes with temperature variation as observed in some skutterudite compounds.[9,10] A similar result was derived and further refined by Hattori and Tsunetsugu[11] for the strongly anharmonic compound KOs_2O_6.[12] Bernstein *et al.*[13] calculate the thermal conductivity of $CoSb_3$ and $LaFe_4Sb_{12}$ by Green-Kubo molecular-dynamics simulations and link the reduced heat transport to anharmonic terms of the low-energy modes only present in the filled compound. These studies highlight in particular the sensitivity of the modelled results to the input parameters that characterize the coupling between the constituents of the compounds and manifest themselves in the microscopic dynamics.

In the present publication we extend and refine our discussion of the microscopic dynamics of $M_{1-x}Fe_4Sb_{12}$, with the divalent cations M = Ca, Sr, Ba, and Yb,[14] to temperature effects, which are measured between 2 and 600 K and to the powder-averaged dynamic structure factor $S(Q,\omega)$, a two-dimensional response function reflecting the form factors of the phonon system. $S(Q,\omega)$ has been mapped out by angle-dispersive INS and inelastic x-ray scattering (IXS) techniques. The computational work is expanded to powder-averaged-lattice-dynamics (PALD) calculations for a comparison with $S(Q,\omega)$. This approach is performed in analogy to the study of $La_{1-x}Fe_4Sb_{12}$ and $Ce_{1-x}Fe_4Sb_{12}$ skutterudites.[5]

Note that due to the abundance of experimental and computational data resulting from the angle-dispersive-spectroscopy techniques and the PALD calculations, we wish to restrict our report to a subset of results only. We have chosen $BaFe_4Sb_{12}$ and $YbFe_4Sb_{12}$ to demonstrate the quality of the experimental and computed $S(Q,\omega)$ and to highlight the excellent match between these two quantities. Any $S(Q,\omega)$ data set obtained with $CaFe_4Sb_{12}$ and $SrFe_4Sb_{12}$ as well as the match of computed with experimental results is of similar quality or better. As has been pointed out in Ref. 6, the inelastic response of $BaFe_4Sb_{12}$ is strongly reminiscent of the properties of $CaFe_4Sb_{12}$ and $SrFe_4Sb_{12}$. A result equivalently elaborated from DFT calculations for Ca-, Sr-, and Ba-filled Co_4Sb_{12} compounds by Wee *et al.*[15] Thus, $S(Q,\omega)$ of $BaFe_4Sb_{12}$ represents, to a good approximation, the general aspects of the phonon properties of Ca- and Sr-filled iron antimonides. Any departure from this behavior is explicitly pointed out and discussed hereafter.

For clarity, we abandon the indication of the cation-filling grade $1-x$ when labeling the measured compounds by their chemical formula MFe_4Sb_{12} with $M =$ Ca, Sr, Ba, and Yb. However, we note that the filling was estimated by Rietveld refinement of neutron-diffraction data to be 94%–98% for any of the measured iron antimonides.[6] The computer-generated structures are 100% filled.

The paper is structured as follows. In Sec. II, we present an introduction to experimental and computational details not reported in the preceding manuscript (see Ref. 6). The presentation of the results in Sec. III is started with the temperature-dependent results of the generalized density of states (see Sec. III A). After a condensed report on phonon-dispersion relations calculated for the main symmetry directions of the studied compounds (see Sec. III B), we continue with a detailed discussion of the dynamic structure factor, $S(Q,\omega)$, reporting INS data and respective PALD calculation results (see Sec. III C). The $S(Q,\omega)$ data are complemented in Sec. III D by results from IXS experiments, mapping out the signal within the reduced first Brillouin zone, and from PALD calculations on Ba- and Yb-filled iron antimonides. A presentation of computed velocity of sound, Debye temperature, and related material constants such as elastic, bulk, and Young's moduli follows in Sec. III E. We finish this work with a discussion of the results, setting their importance in relation to published data, and a summary in Secs. IV and V, respectively.

II. EXPERIMENTAL AND COMPUTATIONAL DETAILS

We refer the reader for details of the sample preparation, the *ab initio* DFT and direct-method phonon calculations, and the high-resolution neutron time-of-flight spectrometer IN6@ILL to Refs. 6, 16, 17 and references therein. All data presented here have been collected with the same samples as in the previous publication.[6]

A. Neutron-scattering time-of-flight experiments

For the present study of vibrational dynamics at very low temperatures, the thermal neutron time-of-flight spectrometer IN4@ILL of the Institut Laue Langevin in Grenoble, France, was used. This spectrometer offers the possibility of monitoring the Stokes spectrum (neutron energy loss) of excitations with the maximum sampled energy being dependent on the incident energy of neutrons. We have exploited IN4@ILL in two setups: for experiments on Ca-, Sr-, and Ba-filled skutterudites, an incident neutron energy of 25.4 meV was chosen with an energy resolution of 1.1 meV (full width at half maximum) at $\hbar\omega \approx 0$ meV. $YbFe_4Sb_{12}$ was studied with an incident energy of 12.9 meV and a resolution of about 0.6 meV at $\hbar\omega \approx 0$ meV. The energy-resolution function is approximately Gaussian. Figure 1 reports the energy-momentum ($\hbar\omega$-Q) phase-space coverage of IN4@ILL achieved with different setups.

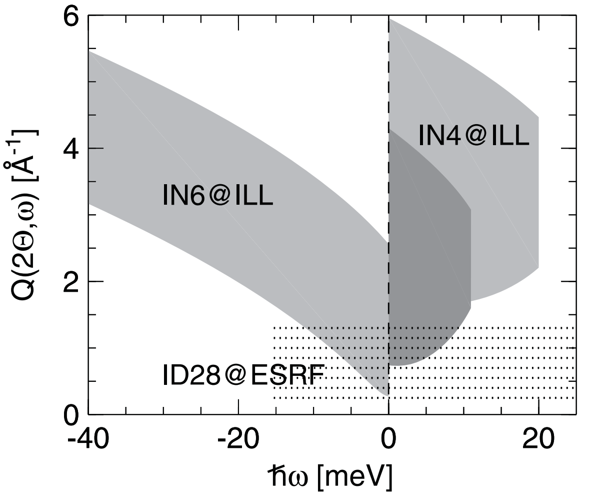

FIG. 1. Phase-space coverage by the neutron time-of-flight spectrometers IN4@ILL (right, Stokes side) and IN6@ILL (left, anti-Stokes side) as they have been exploited for the data analysis. Light-shaded area indicates the IN4@ILL coverage reached with the incident neutron energy of 25.4 meV. Dark-shaded area indicates the coverage with 12.9 meV. Dotted lines sketch the constant Q scans performed with the IXS spectrometer ID28@ESRF.

A standard helium cryostat was used at IN4@ILL. Ca-, Sr-, and Ba-filled iron antimonides were measured at 150 K and base temperature of about 2 K. $YbFe_4Sb_{12}$ was measured at 2, 20, 50, 100, and 200 K. A helium atmosphere of a few millibars was used for thermalization of the samples. IN6@ILL experiments were performed with a standard cryofurnace on Ca-, Sr-, and Ba-filled skutterudites at 150 and 300 K, and at the maximum temperature of about 530 K in a helium atmosphere of 1–10 mbar. $YbFe_4Sb_{12}$ was measured at 300 and 600 K in a heating loop and high vacuum. All measurements were performed in transmission geometry using flat aluminum sample holders oriented at 135° with respect to the incoming neutron beam. Auxiliary data sets for detector calibration and empty-can corrections were taken.

B. Inelastic x-ray experiments

IXS experiments have been performed on the compounds $BaFe_4Sb_{12}$ and $YbFe_4Sb_{12}$ at the high-resolution beamline ID28@ESRF of the European Synchrotron Radiation Facility in Grenoble, France. Like INS the applied IXS technique is sensitive to bulk properties of materials offering, unlike INS, access to the complete first Brillouin zone and hence to their velocity of sound.[18,19] The spectrometer was utilized with an (11.11.11) silicon monochromator setup, giving an energy resolution of 1.6 meV (full width at half maximum) over the entire energy range and a resolution line shape well approximated by a pseudo-Voigt function. In test runs, e.g., employing the (9.9.9) monochromator reflection, the chosen setup proved to be the best option in terms of scattered intensity and signal-to-noise ratio. Nevertheless, the IXS experiment remained an ambitious venture in terms of the counting statistics as the scattered intensity is $\propto Z^2$, with Z the electronic number of the scattering atom, whereas the absorption is enhanced $\propto Z^4$ (see Refs. 18 and 19).

The multianalyzer unit was set to access a momentum Q range of 0.24–1.27 Å^{-1} in transmission geometry covering the first generalized Brillouin zone of the polycrystalline samples and complementing the coverage of the INS experiments. The constant-Q slices mapping out an energy range of -15 to 25 meV are indicated in Fig. 1 as dotted lines. Powdered samples were loaded in 2 mm bores drilled into a steel foil of 100 μm thickness adapted to the absorption length of the compounds. The powder was framed on both sides of the steel foil with kapton foil. Spectra were recorded in a high-vacuum environment at room temperature, exclusively. Equal data-acquisition time was applied for both compounds resulting in comparable statistical accuracy of the spectra. Auxiliary data of resolution functions and empty-container signals were recorded.

C. Data treatment and calculation techniques

Data treatment was performed as in Refs. 5 and 6. For the discussion of spectra at constant momentum transfer, the INS dynamic structure factor $S(2\Theta,\omega)$ has been interpolated to $S(Q,\omega)$. Different binnings have been applied for the different experimental setups, whereby a constant Q binning with a ΔQ corresponding to the elastic Q numbers of $S(2\Theta,\omega = 0)$ was chosen. Additional binning has been performed to data wherever an improvement of statistical accuracy was appropriate. All neutron-weighted generalized densities of states $G(\omega)$ computed from IN6@ILL data have been normalized to equal intensity in the energy range 0.5–40 meV. IN4@ILL data have been scaled onto those from IN6@ILL in terms of intensity in the energy range of interest. The dynamic structure factor $S(Q,\omega)$ of all compounds measured at IN6@ILL has been normalized to equal intensity within the double-peak feature around 30 meV. This normalization procedure is well justified as the intensity of this high-energy band is dominated by eigenmodes with high Sb and Fe amplitudes and is consequently comparable for these compounds.[6,20–22]

Data from the IXS experiment at ID28@ESRF were symmetrized according to the detailed balance of scattering processes and Stokes and anti-Stokes lines were combined to optimize statistics. The elastic intensity was suppressed by taking into account the independently measured resolution function. All spectra shown here are in arbitrary units.

PALD data were derived according to the available INS and IXS data sets. The PALD approach is based on a lattice-dynamics calculated set of eigenmodes i with momentum $\hbar\vec{q}$ and energy $\hbar\omega(\vec{q},i)$ for which the dynamic structure factor $S'(\vec{Q},\omega,T)$ is computed for a large number of $\vec{Q} = \vec{q} + \vec{G}_{hkl}$ with random orientation on a dense equidistant $|\vec{Q}|$ grid. $\vec{G}_{hkl}$ represents the lattice vectors of the crystal. For a phonon, creation process (Stokes line) follows

$$S'(\vec{Q},\omega,T) = \frac{\hbar}{2\omega}\,[1-\exp(-\hbar\omega/k_BT)]^{-1} \times \sum_{\vec{q},\vec{G}_{hkl}} \sum_{\text{i}} \delta[\vec{Q}-(\vec{q}+\vec{G}_{hkl})]\,\delta[\omega-\omega(\vec{q},\text{i})] \times \left|\sum_n \frac{a^n_{\text{coh}}}{\sqrt{M_n}}\,\text{e}^{-W_n(\vec{Q},T)}\,\vec{Q}\cdot\vec{e}(\vec{q},i,n)\right|^2. \quad (1)$$

Index n characterizes the nth atom of mass M_n with the coherent scattering length a^n_{coh}. Its temperature-dependent Debye-Waller factor is given by $\text{e}^{-W_n(\vec{Q},T)}$ and takes full account of the mean–square displacement properties of atom n at a given temperature T within the harmonic approximation (see Ref. 6). The polarization vector of eigenmode i at a point $\vec{q}$ within the 1st Brillouin zone is expressed by $\vec{e}(\vec{q},i,n)$. $[1-\exp(-\hbar\omega/k_BT)]^{-1}$ denotes the thermal occupation number with k_B the Boltzmann constant and delta functions express the momentum and energy conservation of the scattering event. Finally, $S'(\vec{Q},\omega,T)$ is regrouped according to an adjustable $\Delta|\vec{Q}|$ and $\Delta\omega$ binning and orientationally averaged to $S'(Q,\omega,T)$.

Neutron-weighted signals have been computed for all compounds in the Q range 0–5 Å^{-1} with a^n_{coh} the tabulated coherent scattering lengths.[6,23] X-ray weighted signals have been computed for $\text{BaFe}_4\text{Sb}_{12}$ and $\text{YbFe}_4\text{Sb}_{12}$. For the low-$Q$ regime inspected here, the scattering length a^n_{coh} has been approximated by the x-ray form factor $f(Q \to 0)$ being proportional to the electronic number Z_n of atom n, i.e., $Z_{\text{Fe}} = 26$, $Z_{\text{Sb}} = 51$, $Z_{\text{Ba}} = 56$, and $Z_{\text{Yb}} = 70$.[18,19]

For the discussion of IXS spectra, it is noteworthy here that within the 1st Brillouin zone the scattered intensity is determined by basic selection rules. For $\vec{G}_{hkl} = 0$, the scalar product $\vec{Q}\cdot\vec{e}(\vec{q},i,n)$ allows only longitudinal modes with $\vec{Q} \parallel \vec{e}(\vec{q},i,n)$ to be detected. The detectability of transverse eigenmodes with $\vec{Q} \perp \vec{e}(\vec{q},i,n)$ is appreciably suppressed. Another selection rule is given by the summation over all n atoms in a unit cell, canceling out intensities of eigenmodes determined by oppositely phased $\vec{e}(\vec{q},i,n)$ and, hence, of optic phonons.[24,25] Consequently, for $Q \to 0$ only the acoustic phonon of longitudinal polarization is detectable.

Calculated $S'(Q,\omega,T)$ spectra have been adapted to the experimental signal by taking into account the temperature, Stokes or anti–Stokes scattering events, and the instrumental resolution functions. INS-weighted spectra have been convoluted with a Gaussian whose energy-dependent width follows the resolution of direct time-of-flight instruments equipped with a monochromator.[26,27] IXS-weighted spectra have been convoluted with the experimentally determined resolution function. For clarity reasons we refer to the PALD-computed $S'(Q,\omega,T)$ as $S(Q,\omega)$ hereafter.

III. RESULTS

A. Temperature response of the generalized density of states $G(\omega)$

Figure 2 shows the generalized density of states $G(\omega)$ of all compounds measured at different temperatures. In the

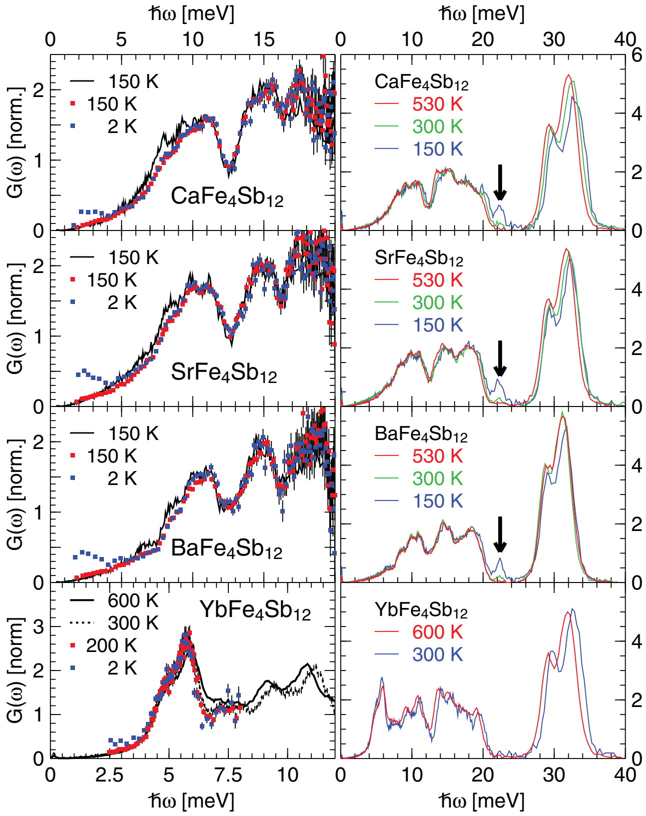

FIG. 2. (Color online) Temperature dependence of the generalized density of states, $G(\omega)$, of Ca-, Sr-, Ba-, and Yb-filled Fe_4Sb_{12} compounds measured at IN4@ILL (symbols) and IN6@ILL (lines). Temperatures are color-coded and reported in the figures. Left, a close-up look at the low-energy range of $G(\omega)$. Note the different energy scale of the $YbFe_4Sb_{12}$ data. At 2 K the strong elastic contribution from the manifold of Bragg reflections of the polycrystalline samples obscures the inelastic signal of Ca-, Sr-, and Ba-filled skutterudites below 4 meV. Right, entire energy range of $G(\omega)$. Vertical arrows indicate the second-order elastic scattering from the monochromator of IN6@ILL becoming detectable at low temperatures.

left panel, a direct comparison of IN4@ILL with IN6@ILL data is made possible in the low-energy range of vibrational excitations. Note that differences in phase-space coverage and resolution of the instruments, which are discussed in the preceding section, lead to subtle differences in $G(\omega)$ obtained from the two spectrometers as seen in the data sets at 150 K of the Ca, Sr, and Ba compounds.

The obvious effect of temperature changes is the shift of the entire $G(\omega)$ toward lower energies upon heating, best seen in the positions of the Fe-dominated band around 30 meV. This anharmonic trend is as well detectable in the shift of the Sb-dominated bands below 20 meV and revealed in the close-up view on the temperature response of the low-energy modes of $YbFe_4Sb_{12}$ in the bottom left part of Fig. 2. The Fe-dominated double peak feature has been approximated by two Gaussians and the resulting energy fit parameters of the two peaks are listed in Table I. A stronger softening of the Ca- and Yb-filled than of the Sr- and Ba-filled iron antimonides can be conjectured from the behavior of the energy parameters.

TABLE I. Energy, in meV, of the two high-energy Fe-dominated peaks identified by Gaussian fits to $G(\omega)$ calculated from IN6 data. Note that $YbFe_4Sb_{12}$ was measured at 600 K.

	530/600 K		300 K		150 K	
	E_1	E_2	E_1	E_2	E_1	E_2
Ca	29.1(1)	32.01(4)	29.5(1)	32.56(5)	29.8(1)	33.0(1)
Sr	28.9(1)	31.7(1)	29.0(1)	31.9(1)	29.2(1)	32.3(1)
Ba	28.7(1)	31.3(1)	28.6(1)	31.2(1)	29.0(2)	31.6(1)
Yb	29.0(1)	31.89(5)	29.6(1)	32.7(1)		

In contrast to the low-energy response $\hbar\omega \lesssim 12$ meV of Ca-, Sr-, and Ba-filled skutterudites, which does not show any deviation from the general softening trend, the temperature response of the strongly Yb-dominated signal around 5 meV is less clear. Note that, in particular, the softening of the peak centered around 7.5 meV and separated from the Yb-dominated signal at $T \lesssim 300$ K (dotted line in Fig. 2) causes an apparent renormalization of the signal at 600 K (solid line in Fig. 2).

To shed light on the T dependence of the Yb-dominated double peak, we have attempted to approximate $G(\omega)/\omega^2$ by a function comprising two Gaussians and a background term. See Ref. 28 for details of the fit. $G(\omega)/\omega^2$ monitors sensitively departures from a Debye characteristics for which $G(\omega)/\omega^2 =$ const. It is displayed with the fit results in Fig. 3. Note the strongly ascending intensity toward low energy. It stems from the elastic contribution of the Bragg peaks becoming progressively prominent toward lower T as the occupation number $[1 - \exp(-\hbar\omega/k_BT)]^{-1}$ reduces the inelastic signal. Apart from the changing elastic contribution, no clear variation of the inelastic signal is obvious within the range of the double-peak feature. Only at $T = 600$ K the double peak appears to be reduced in intensity, however, broadened.

All fit parameters of the Gaussian lines, i.e., energy E of the peaks, their full width at half maximum $\gamma = 2\sigma\sqrt{2\ln 2}$, amplitude A, and the intensity $I = A\sigma\sqrt{2\pi}$ are shown in Fig. 4. Note that the application of two different experimental setups necessitates due care when comparing γ and A derived

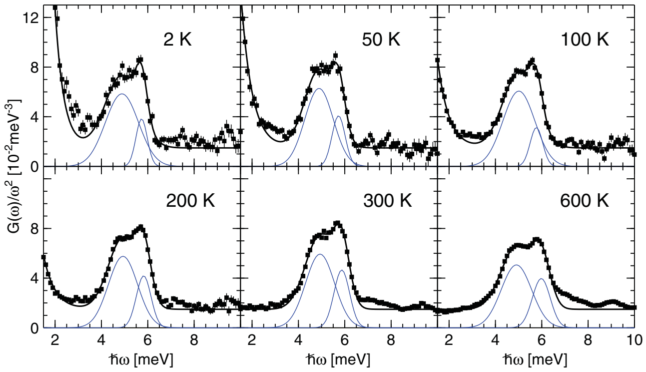

FIG. 3. (Color online) Low-energy range of $G(\omega)/\omega^2$ of $YbFe_4Sb_{12}$ at different temperatures indicated in the figures. Black full lines indicate fit results as discussed in the text. Blue full lines highlight the partial contribution by the two applied Gaussians. Fit parameters are reported in Fig. 4.

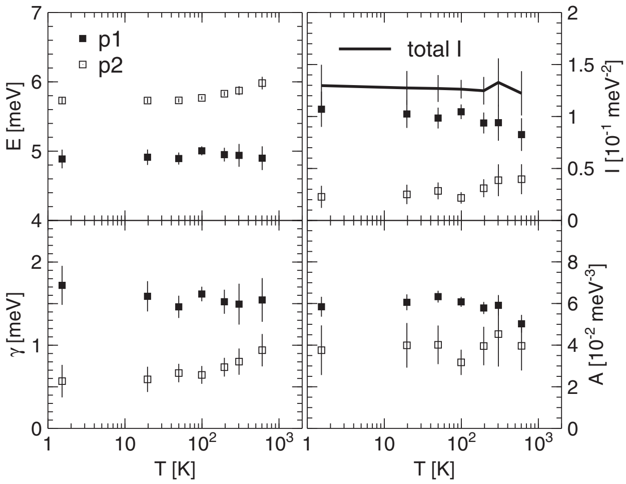

FIG. 4. Fit parameters, energy E, full width at half maximum γ, amplitude A, and intensity I of the two Gaussians fitted to the double-peak feature in $G(\omega)/\omega^2$. Full and empty squares characterize the low-energy (p1) and high-energy (p2) peaks, respectively. Full line represents the total intensity.

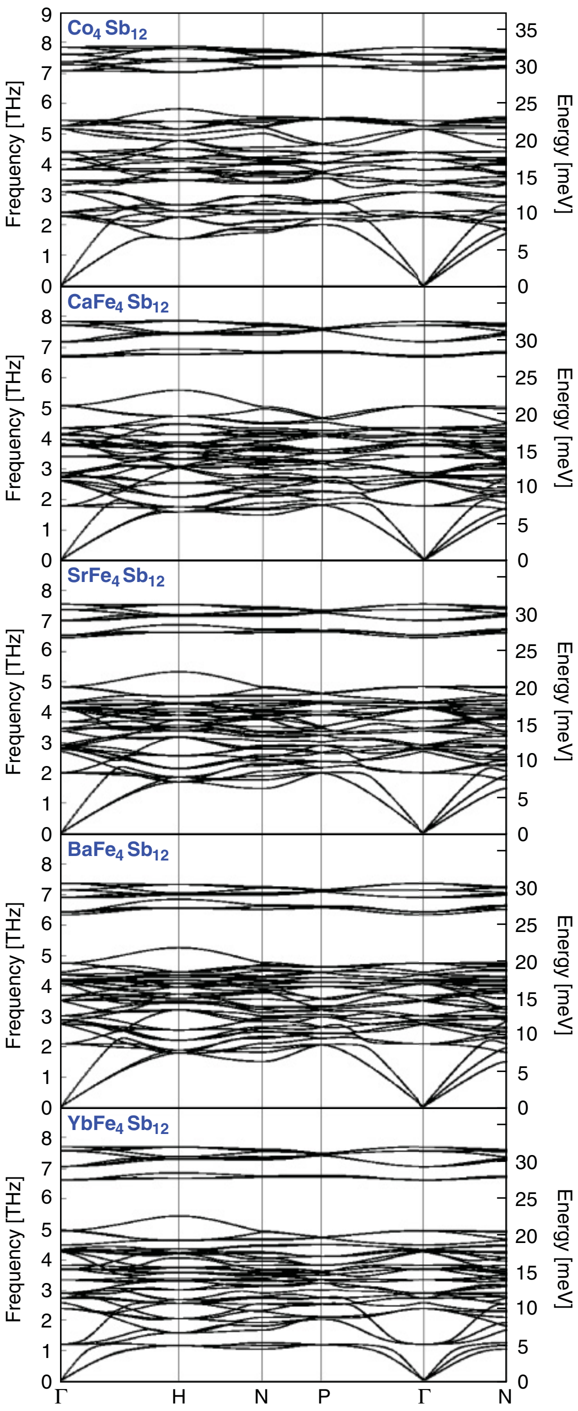

FIG. 5. From top to bottom, phonon dispersion relation of CoSb$_3$ and Ca-, Sr-, Ba-, and Yb-filled iron antimonides calculated along the main symmetry directions.

from IN6@ILL and IN4@ILL data. Only the E and, under the condition of a sufficient incoherent approximation, the I parameters are robust numbers. The behavior of the integrated intensity indicates a progressive shift of the spectral weight from the low-energy peak 1 to the high-energy peak 2 for $T \gtrsim 200$ K, whereby the total intensity of the two Gaussians is weakly reduced between 2 and 600 K. With the shift of the spectral weight, a frequency shift of the high-energy peak 2 is indicated by the fit results. The energy of the low-energy peak 1 does not show any shift upon T variation. A discrimination between a possible physical origin of the shift and a numerical artefact is not straightforward due to the necessary number of fit parameters and the reduced characteristics of the peak profile.

The conclusions upon the energy shift can be however expanded onto the Q-resolved signal monitored with the same experimental setup at IN6@ILL. In Fig. 9, we anticipate results from equivalent fits to the INS $S(Q,\omega)$ data as it will be discussed in the proceeding chapter. The Q-resolved data confirm the stronger response of the peak at higher energy to T changes displaying a blue shift and contrasting the red shift of the Fe- and Sb-dominated signal upon heating. Within the data accuracy we can not identify specific Q points at which this energy shift would be particularly amplified or suppressed compared to other Q points.

B. Calculated phonon dispersion

Figure 5 depicts the phonon dispersion of the ternary-filled skutterudites studied and of the binary CoSb$_3$ skutterudite calculated along high-symmetry directions.

Ca-, Sr-, and Ba-filled iron antimonides show, besides a subtle renormalization of eigenfrequencies, a common phonon scheme. The renormalization follows the systematics established from experimental data discussed in Ref. 6. Following the sequence of Ca-Sr-Ba filled iron antimonides, low-energy cation-dominated eigenmodes display a progressive blue shift whereas high-energy iron-dominated eigenfrequencies show a redshift. This shift can be best evaluated from the distribution of Γ-point frequencies (see also Table V in Ref. 6). It highlights the dominant effect of the bonding properties of the cation to the anionic matrix rather than the mass of the cation on the frequencies of collective excitations of the compounds. However, as far as the behavior of eigenmodes of lowest energy at the zone boundary is concerned, the blue shift is less prominent than at the Γ point, zone center. Consequently, a smaller splitting of Γ-point energies of lowest

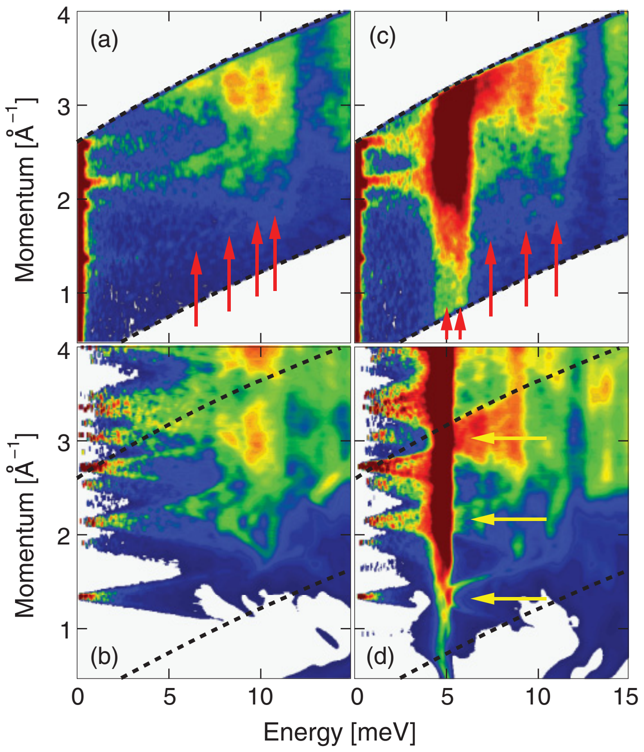

FIG. 6. (Color) Contrast plot of the dynamic structure factor of $BaFe_4Sb_{12}$ (a) and $YbFe_4Sb_{12}$ (c) measured at 300 K. Figures (b) and (d) report the corresponding PALD-calculated signals. The low-energy part of the spectra, dominated by eigenmodes with a strong contribution of the M cations, is highlighted. Red vertical arrows indicate peaks identified in the inelastic response of the compounds.[6] Yellow horizontal arrows highlight Γ points at which the symmetry-avoided anticrossing of phonon modes is observable in the PALD signal. Black dashed lines span the limits of the energy-momentum phase space of the IN6@ILL experiment. Note that the intensity of the Yb-dominated modes has been chosen to saturate the color resolution, enabling a better visualization of the overall signal.

optic modes and zone-boundary van Hove singularities is calculated, for example, for $CaFe_4Sb_{12}$ than for $BaFe_4Sb_{12}$. The results obtained here are in agreement with experimental and computational studies of the binary structure in Refs. 20, 29, 30 and of filled cobalt antimonides in Ref. 15. Also in agreement with Ref. 15 is the observation that at specific $\vec{Q}$ points, localization of eigenmodes sets in at lower energies in the binary $CoSb_3$ compound than in the ternary-filled iron antimonides. The weak dispersion around the high-symmetry H point is a clear example of this eigenmode localization at which the group velocity $\partial\omega(Q)/\partial Q \approx 0$ in an extended Q range.

A pronounced renormalization of eigenmodes is observed for $YbFe_4Sb_{12}$ as a fundamental change in the dispersion behavior of the low-energy phonons. In contrast to a Debye-like back-folding effect of acoustic phonons at the Brillouin zone boundary, the low-energy eigenmodes in $YbFe_4Sb_{12}$ display globally a symmetry-avoided anticrossing dispersion. However, a discrimination of the phonon dispersion into back-folded or anticrossing is neither adequate in the case of Ca-, Sr-, and Ba-filled iron antimonides nor appropriate to characterize the collective dynamics of the binary system. Judging from our lattice dynamics calculations, back-folding or anticrossing is a question of eigenmode symmetry and dispersion direction and both terms are applicable to characterize the low-energy modes of Ca-, Sr-, and Ba-filled iron antimonides. The dispersion relation along Γ-N, as displayed in Fig. 5, can be taken as an example of the dispersion complexity. This statement can be expanded to studies of the low-energy phonon properties of the binary $CoSb_3$ compound and of $LaFe_4Sb_{12}$.[5,20,29–32]

C. Angle-dispersive inelastic neutron scattering

Contrast plots of the inelastic signal of Ba- and Yb-filled skutterudites measured at IN6@ILL and PALD calculated are reported in Fig. 6. The experimental spectra plotted in the top figures are taken at 300 K and normalized to the same intensity of the Fe-dominated high–energy modes. Van Hove singularities in $G(\omega)$, indicated by vertical arrows, are listed and discussed in Ref. 6.

Two features are worth noting. Van Hove singularities, well distinguished in the Q-averaged response of $G(\omega)$, are observable as intensity maxima located in distinct regions of the Q-resolved $S(Q,\omega)$ signal. Additionally, there is an overall intensity variation dependent on the filler species. This variation is due to the scattering power of the M cations (Ca = 70.6 mb/a.m.u., Sr = 71.3 mb/a.m.u., Ba 24.6 mb/a.m.u., and Yb = 134.5 mb/a.m.u.). The intensity of acoustic phonons, visualised, for example, as two horizontally dispersing streaks originating from 0 meV above 2 Å^{-1}, reflects the scattering power variation. For example, the strong difference, around 3 meV, in the $BaFe_4Sb_{12}$ and $YbFe_4Sb_{12}$ data indicate a strong hybridization of M cations with Fe_4Sb_{12} dynamics.

In addition to a convolution with a Gaussian, following the energy resolution of the IN6@ILL time-of-flight spectrometer, a smoothing of data in Q has been applied. Note that unlike the measured data, the PALD-calculated signal is not perturbed by incoherent scattering and by experimental artefacts such as a base noise level and the resolution ellipsoid. Qualitatively, all prominent features of the measured signal are well captured by the PALD calculation.

To substantiate this statement, we show some selected $S(Q,\omega)$ spectra in Figs. 7 ($YbFe_4Sb_{12}$) and 8 ($BaFe_4Sb_{12}$). Any other cross sections of the measured and calculated data are of comparable match and quality and are represented by the results reported on $LaFe_4Sb_{12}$.[5] The spectra have been Q-averaged over $\Delta Q = 0.1$ Å^{-1}, and Q points have been chosen for the most characteristic features in $S(Q,\omega)$. The notation of arbitrary units for the intensity applies only to the scaling of measured with respect to calculated data sets. The intensity of each of the sets, experimental on the one hand and PALD on the other, are in equivalent units and directly comparable.

An overall good match of measured and calculated $S(Q,\omega)$ is evident and the characteristic energies and intensities of distinct peaks and their variation with Q changes are well reproduced. The most obvious difference can be found within the intense Yb-dominated modes in Fig. 7. The PALD calculation underestimates slightly the average energy and the width of this mode band. Insets in the right panel of Fig. 7 offer a close-up view of the simulated peak and highlight the intensity distribution and its variation with Q within this peak.

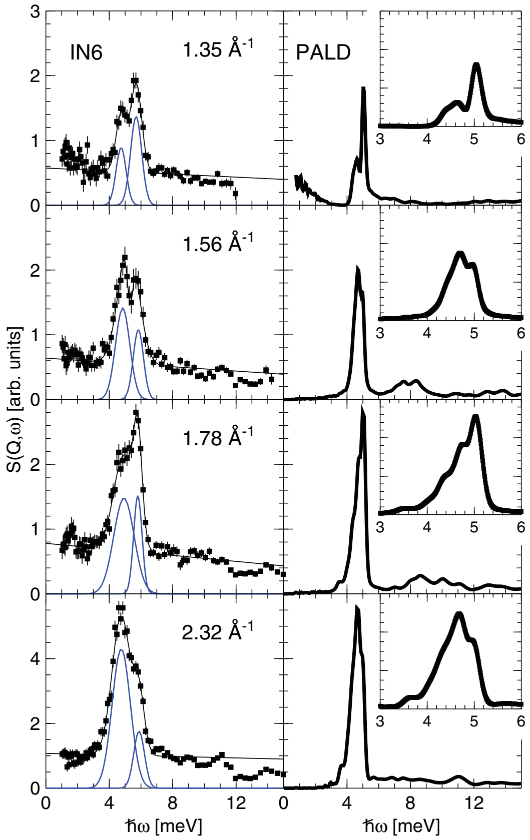

FIG. 7. (Color online) Measured (left) and PALD-calculated (right) constant Q spectra $S(Q,\omega)$ of $\mathrm{YbFe_4Sb_{12}}$. Wave numbers Q are reported in the figures. Lines represent fits to the apparent double-peak feature with the bulk Gaussian response peaks (blue). The insets highlight the line shape of the strong peaks.

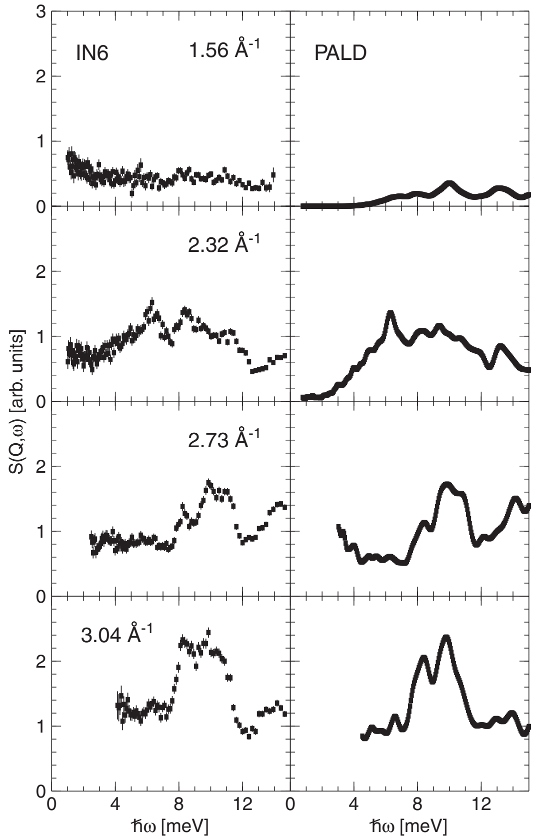

FIG. 8. Measured (left) and PALD-calculated (right) constant Q spectra $S(Q,\omega)$ of $\mathrm{BaFe_4Sb_{12}}$. Wave numbers Q are reported in the figures.

This variation follows closely the changes of the measured intensity distribution obtained by fitting with two Gaussians. Fit results are indicated by full lines in the figure. Note that the resolution-convoluted PALD signal reveals that a double-peak description is not an adequate approximation to the signal. Indeed, sound indications for a more complex lineshape can be found at some Q points of the resolution-affected experimental data here as well as in the results of $\mathrm{LaFe_4Sb_{12}}$.[5]

As indicated in the preceding section, parameters of the Q-resolved fits have been summarized in Fig. 9. With $E(Q)$, $\gamma(Q)$, and $I(Q)$ the relative intensity of the two peaks $I_{\mathrm{rel}}(Q) = I(\mathrm{p1},Q)/I(\mathrm{p2},Q)$ at corresponding temperatures is reported. Additionally, the structure factor $S(Q_{\mathrm{elastic}}) = \int S(2\Theta,\omega)\mathrm{d}\omega$ with $Q_{\mathrm{elastic}} = Q(2\Theta,\omega = 0)$ is displayed with the $\gamma(Q)$ and $I_{\mathrm{rel}}(Q)$ data. Despite the numerical accuracy of the fit parameters, a trend of $\gamma(Q)$ to be lightly enhanced at 600 K is visible. Also, a decrease of intensity is obvious from the total numbers of $I(Q)$ being enhanced toward higher Q, as might be expected from the effect of the Debye-Waller factor. These observations are in agreement with the results reported in Fig. 4.

There is one noteworthy feature left to be highlighted. At Q points corresponding to Γ points highlighted by the Bragg reflections in $S(Q_{\mathrm{elastic}})$, the widths $\gamma(Q)$ and $I_{\mathrm{rel}}(Q)$ of the two modes display a pronounced modulation. The low-energy peak p1 becomes visibly narrower as well as weaker when compared to the property of p2. These effects are particularly enhanced at Q points of about 1.4 and 3 Å^{-1} and result from the symmetry-avoided-anticrossing dispersion in $\mathrm{YbFe_4Sb_{12}}$. In a powder sample, the modulation of $\gamma(Q)$ and $I_{\mathrm{rel}}(Q)$ is less evident due to averaging over different Brillouin-zone points matching the modulus $Q = |\vec{Q}| = |\vec{q} + \vec{G}_{hkl}|$. It is, as well, progressively obscured with increasing Q as more and more $\vec{G}_{hkl}$ satisfy the momentum-conservation condition and contribute to the signal.

D. Inelastic x-ray scattering

Figure 10 displays a selected set of IXS spectra and PALD results calculated for corresponding conditions.

We define the boundary of the 1st reduced Brillouin zone as $Q_{1.\mathrm{rBZ}} = |\vec{G}_{110}|/2$ with $|\vec{G}_{110}|$ the position of the first allowed Bragg reflection in skutterudite structures. It is indicated by a horizontal yellow arrow in the PALD data of $\mathrm{YbFe_4Sb_{12}}$ in Fig. 10. From our experiments and calculations $Q_{1.\mathrm{rBZ}} \approx 0.5$ Å^{-1}. According to selection rules imposed by Eq. (1) and indicated in Sec. II C, the PALD-derived signal is dominated by the acoustic mode of longitudinal polarization at $Q \to 0$ in both compounds. In the case of $\mathrm{YbFe_4Sb_{12}}$, the hybridization of the acoustic and the low-energy optic mode allows the detectability of two modes above their crossing point $\hbar\omega \gtrsim 5$ meV and $Q \gtrsim 0.25$ Å^{-1}. Since in $\mathrm{BaFe_4Sb_{12}}$ eigenmode localization, back-folding and/or anticrossing take place at

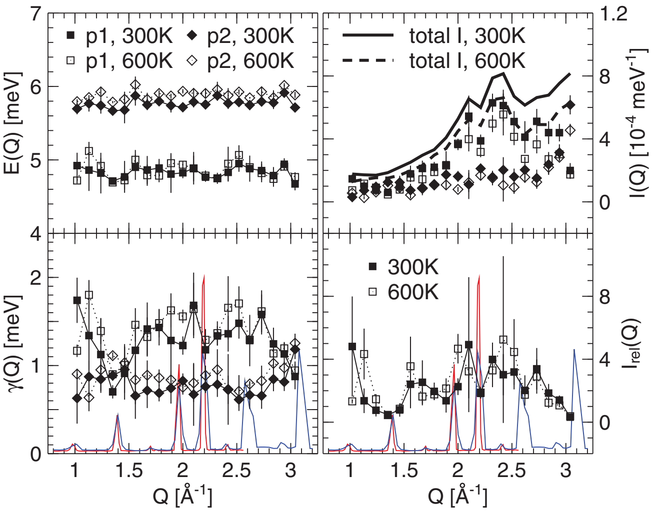

FIG. 9. (Color online) Q-resolved energy $E(Q)$, full width at half maximum $\gamma(Q)$, intensity $I(Q)$, and relative intensity $I_{\text{rel}}(Q)$ parameters of the two Gaussian peaks (p1 and p2) fitted to the low–energy signal of $YbFe_4Sb_{12}$ measured at IN6@ILL. Symbols and lines applicable to $E(Q)$, $\gamma(Q)$, and $I(Q)$ are defined in the top figures. Symbols for $I_{\text{rel}}(Q)$ data are defined in the corresponding figure. Red and blue lines represent the structure factor $S(Q_{\text{elastic}})$ as detected at IN6@ILL and IN4@ILL, respectively.

higher energies and hence higher Q, only the longitudinal acoustic phonon below any localization point can be observed as a single peak. Finally, when crossing $Q_{1.\text{rBZ}}$ from $Q = 0.39$ to 0.54 Å^{-1}, the spectra display additional complexity, which is reflected by the multiplicity of peaks becoming detectable at $\hbar\omega \gtrsim 10$ meV.

Despite the reduced statistical accuracy of the experimental data, some of the prominent features computed by the PALD technique are detectable in the IXS data. These features comprise the evolution of the spectral distribution with increasing Q, matching the evolving complexity of $S(Q,\omega)$, as well as the dispersive character of a few distinguished peaks. Energies of the primary peaks obtained from fitting a set of Gaussians to the data within the 1st reduced Brillouin zone are indicated by large white circles in Fig. 10 and listed in Table II. Small circles indicate peaks of weak but detectable intensity. In principle, the energy variation of the low-energy modes is captured by the fit results matching qualitatively the behavior of the PALD results. Note, however, that details in the spectral profile cannot be identified unequivocally beyond a $Q > 0.7$ Å^{-1}, raising appreciably the uncertainty parameters of the fits. Rather wide featureless bands of enhanced intensity are present in the experimental data and have been indicated by the dashed lines in Fig. 10.

Interpreting the energy points indicated by the white horizontal arrows at $Q = 0.24$ Å^{-1} ($YbFe_4SB_{12}$: $E = 7.0 \pm 0.4$ meV, $BaFe_4Sb_{12}$: $E = 6.8 \pm 0.2$ meV) as being determined by the longitudinal velocity of sound, v_l, we obtain $v_l = 4400 \pm 250$ and 4270 ± 130 m/sec for $YbFe_4Sb_{12}$ and $BaFe_4Sb_{12}$, respectively. However, we have to highlight that, from close inspection of the PALD-computed spectra in the vicinity of $Q = 0.24$ Å^{-1}, the dispersion of the longitudinal acoustic phonon in $BaFe_4Sb_{12}$ shows a departure from a strict linear dependence $\hbar\omega(Q) \propto Q$. Hence, the v_l calculated from the measured spectra underestimates the true v_l of $BaFe_4Sb_{12}$. For $YbFe_4Sb_{12}$, the PALD-calculated spectra indicate that linearity in the energy-momentum relation is re-established

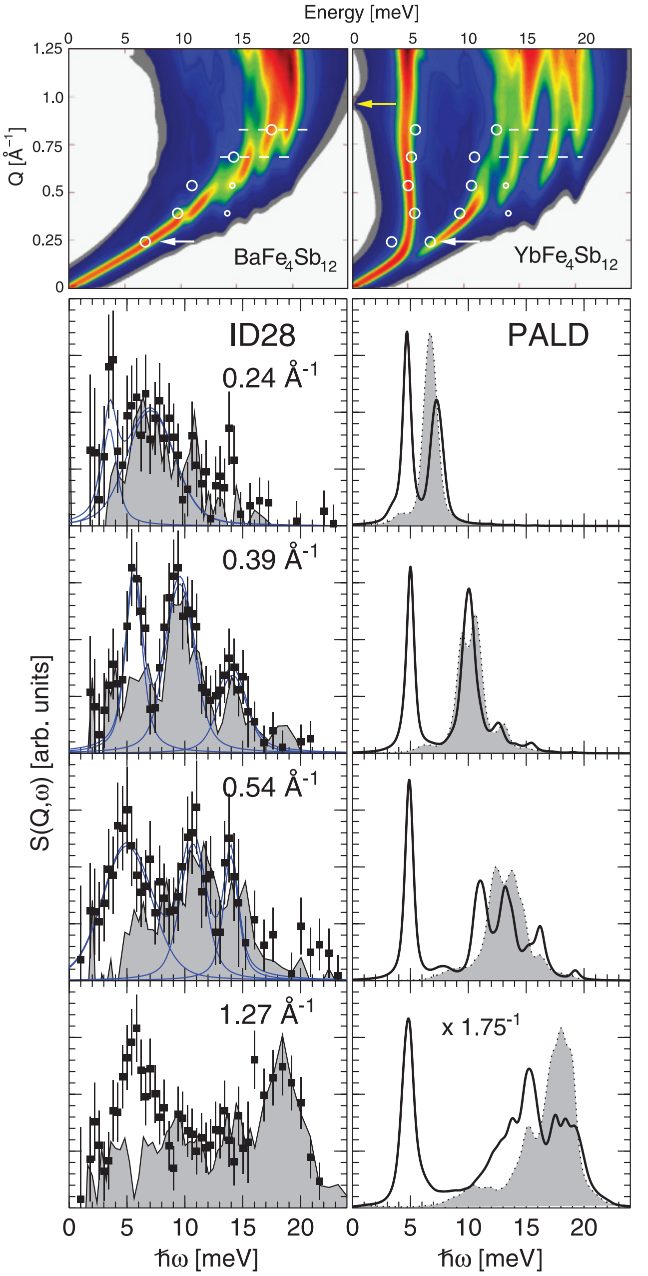

FIG. 10. (Color) Figures on top display contrast plots of IXS-weighted PALD-caclulated $S(Q,\omega)$ of $BaFe_4Sb_{12}$ and $YbFe_4Sb_{12}$ skutterudites. Panels below report constant Q cuts through the measured (left) and PALD-calculated (right) data. Wave numbers Q are reported in the figures. $YbFe_4Sb_{12}$ data are represented by full symbols with error bars (left) and full lines (right). $BaFe_4Sb_{12}$ data are represented by the grey shaded area. The statistical accuracy of the experimental results is comparable to the one of $YbFe_4Sb_{12}$. Solid (blue) lines demonstrate fitting results approximating the signal by a set of Gaussian lines convoluted with the resolution function. The resulting energy parameters of the fits are indicated as white circles in the top figures. See text for details.

TABLE II. Energies of the low-energy peaks of $BaFe_4Sb_{12}$ and $YbFe_4Sb_{12}$ skutterudites detected by IXS and approximated by Gaussian lines as presented in Fig. 10.

Q (Å^{-1})	E_1^{Yb} (meV)	E_2^{Yb} (meV)	E_1^{Ba} (meV)
0.24	3.5(1)	7.0(4)	6.8(2)
0.39	5.6(1)	9.6(1)	9.8(1)
0.54	5.0(1)	10.7(1)	11.1(3)
0.69	5.3(2)	11.0(5)	14.9(4)
0.83	5.8(4)	13(2)	18.3(2)

at $Q = 0.24$ Å^{-1}, i.e., above the anticrossing regime, with a v_l well comparable to the value close to zero momentum.

E. Velocity of sound and material properties

The PALD computation approach can be furthermore exploited for a calculation of the microscopic longitudinal (v_{l}) and transverse (v_{t}) velocity of sound, Debye temperature, Θ_{D}, and material properties such as the elastic c_{11}, G, the bulk B, and Young's E moduli. As a first step, we have generated a set of $S(Q,\omega)$ in the momentum range 0–0.3 Å^{-1} with a very high density of $\vec{Q}$ points (2.5×10^5Å^{-1}). Velocities v_{l} and v_{t} have been derived after, for two discrete energy points $\hbar\omega = 1$ and 2 meV and a single $Q = 0.0625$ Å^{-1} under the assumption of a $\hbar\omega(Q) \propto Q$ dependence as first moments of $\langle\omega\rangle = \int S'_{\mathrm{t,l}}(Q = 0.0625\text{ Å}^{-1},\omega)\omega d\omega$ and $\langle Q\rangle = \int S'_{\mathrm{t,l}}(Q,\omega = 1\,\mathrm{meV};\, 2\,\mathrm{meV})Q dQ$. The function $S'_{\mathrm{t,l}}(Q,\omega)$ denotes the spectral densities of the longitudinal and transverse modes normalized to unity. A crosscheck on Θ_{D} has been performed from the low-energy part of the phonon density of states $Z(\omega)$ derived from the standard lattice-dynamics calculation. $Z(\omega)$ was computed on a 10^6 $\vec{Q}$-point mesh to guarantee sufficient statistics at energies down to 0.5 meV. The mathematical relations between v_{l}, v_{t}, $\bar{v}$, Θ_{D}, and $Z(\omega)$ are derived from the Debye model of harmonic solids.[33]

This calculation procedure is sketched in Fig. 11. Examples of the PALD data of $BaFe_4Sb_{12}$ and $YbFe_4Sb_{12}$ are reported in Figs. 11(a) and 11(b) and Figs. 11(c) and 11(d), respectively. Plots (b) and (d) at the bottom show the same data sets as in plots (a) and (c), but with limited intensity to highlight the weak intensity of transverse acoustic phonons. Figures 11(e) and 11(f) report selected $Z(\omega)$ and $Z(\omega)/\omega^2$ plots with dashed lines representing Debye fits $Z(\omega) = A\omega^2$ in the energy range 0.5–1.5 meV.

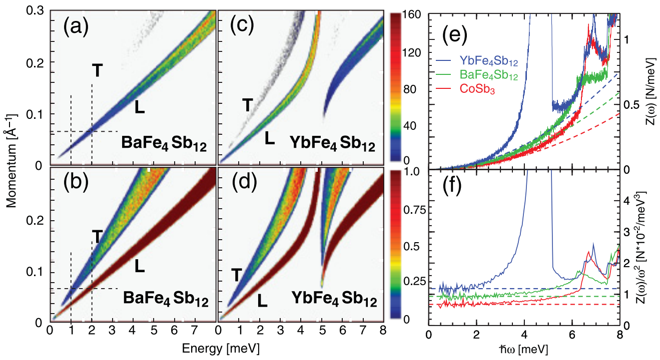

FIG. 11. (Color) Contrast plots of PALD results of $BaFe_4Sb_{12}$ [(a) and (b)] and $YbFe_4Sb_{12}$ [(c) and (d)], $Z(\omega)$ (e) and $Z(\omega)/\omega^2$ (f) of compounds indicated in the figures. Color codes characterizing the intensity in (a) and (c) and (b) and (d) are shown to the right of (c) and (d), respectively. Plots (a) and (b) and (c) and (d) display same data sets on a linear intensity scale, however, intensity in (b) and (d) has been limited to unity to highlight the weak signal of tranverse acoustic phonons (T) in comparison to modes of longitudinal polarization (L). Dashed lines in (a) and (b) indicate lines along which the first moments $\langle\omega\rangle$ and $\langle Q\rangle$ have been calculated. Dashed lines in (e) and (f) represent the results of the Debye fit to the data.

Concise information on the velocity of sound, Debye temperatures, and material properties is given in Table III. Note that all numbers v_{t}, v_{l}, Θ_{D}, elastic constants c_{11}, $c_{44} = G$, Young's modulus E, bulk modulus B, and Poisson's ratio ν have been calculated as mean values of the three $\langle Q\rangle$- and $\langle\omega\rangle$-based velocity of sound data. The precision, given in brackets, has been calculated as the standard deviation from the mean values. Also reported are the lattice parameters as obtained from the DFT calculations and applied for the calculation of the elastic constants.

There is an overall trend of sound velocities and Debye temperatures towards reduced values in the filled skutterudites studied here. Following the behavior of v of the alkaline–earth filled skutterudites in the sequence of cations in ascending mass order shows that the bonding potential (see Ref. 6) counterbalances the mass effect, leading to ascending velocities for Ca-, Sr-, and Ba-filled Fe_4Sb_{12}, respectively. A difference is detectable between the PALD-calculated average sound

TABLE III. Velocity of sound, Debye temperatures, and material properties of $CoSb_3$ and $M Fe_4Sb_{12}$ (M = Ca, Sr, Ba, and Yb) compounds. Values of $\bar{v}_{\mathrm{DL}}$ and Θ_{DL} have been computed from the Debye-level $Z(\omega)/\omega^2$ results from standard lattice-dynamics calculations. All other data have been obtained as mean values of the $\langle Q\rangle$- and $\langle\omega\rangle$-based PALD calculations. The binary compound $CoSb_3$ is labeled by Co, ternary skutterudites are labeled by the cation M.

	d [Å]	$\bar{v}_{\mathrm{DL}}$ [m/s]	Θ_{DL} [K]	v_{t} [m/s]	v_{l} [m/s]	Θ_{D} [K]	c_{11} [GPa]	G [GPa]	E [GPa]	ν	B [GPa]
Co	9.096	3094	322	2929(45)	4719(20)	336(4)	167(1)	64(2)	152(3)	0.19(1)	81(1)
Ca	9.180	2679	278	2637(44)	4487(31)	307(4)	149(2)	51(2)	127(3)	0.24(1)	80(1)
Sr	9.210	2707	281	2646(50)	4462(30)	307(4)	150(2)	53(2)	130(4)	0.23(1)	80(1)
Ba	9.240	2769	288	2703(47)	4479(28)	312(4)	154(2)	56(2)	136(4)	0.21(1)	80(1)
Yb	9.176	2541	264	2475(72)	4263(30)	289(6)	145(2)	49(3)	122(5)	0.25(2)	80(2)

velocity and values obtained from the Debye level $Z(\omega)/\omega^2$. This departure is not unexpected since the PALD results are based on an intensity distribution specifically approximating results from a scattering experiment.

For the binary $CoSb_3$ compound, reference Θ_D values of 307, 319, 321, and 327 K are reported in, or can be calculated from results in Refs. 34–37, respectively. Our present results [$\Theta_{DL} = 322$ K and $\Theta_D = 336(4)$ K] correspond reasonably well to those data, whereby the PALD data are to be understood as property of immaculate specimen. A comparison of results on the filled compounds is however made difficult by incomplete reference data. Zhang *et al.* reports in Ref. 38 on an extensive study of elastic constants of filled iron and cobalt antimonides upon variation of the filling ratio, of the cation filler and of mixtures of cation fillers. Taking into consideration only iron antimonides with high filling ratios, a clear decrease of Θ_D is established as captured in our calculations. We highlight, as an example, the results on $Ca_{0.75}Fe_4Sb_{12}$ ($\Theta_D = 300$ K, Zhang *et al.*) and $CaFe_4Sb_{12}$ [$\Theta_D = 307(4)$ K, present data].

IV. DISCUSSION AND CONCLUSIONS

Let us summarize the two main conclusions that can be reliably drawn from the present data before going into a detailed discussion. We have demonstrated that the vibrational dynamics of Ca-, Sr-, Ba-, and Yb-filled iron antimonides as derived from INS and IXS on powder materials can be well approximated by a set of normal modes obtained from DFT lattice-dynamics calculations. The good match of the PALD calculated with the measured dynamic structure factor $S(Q,\omega)$ indicates that not only the dispersion relations but also the eigenvectors have been reproduced satisfactorily. Moreover, it has been shown by experiments that a moderate softening of the vibrational density of states is induced by heating. Only in the case of $YbFe_4Sb_{12}$, a weak blue shift upon heating of the peak around 5.7 meV, which is identified as an infrared-active (Tu) zone-center mode (see Ref. 6), could be conjectured.

When pointing to the good match of measured and calculated data, it is necessary to point also to some variant features. A slight overestimation of lattice parameters, underestimation of eigenfrequencies, and an overestimation of localization effects in the low-energy range of Yb- and La-filled Fe_4Sb_{12} are recalled as examples.[5,6] This variance is due to the precision of DFT for the specific approach applied (e.g., see Ref. 39 and references therein). The full relaxation of the computer-generated structures and the independence from experimental results is a part of this approach. Hence, a further optimization of the match of experimental and calculation data could be performed on the DFT level or of the dynamical matrix in the lattice-dynamics calculation. The velocity of sound, Debye temperatures, and elastic properties have been derived in this work from the pristine DFT results via PALD. In general, the precision of the present DFT lattice-dynamics calculations is comparable to recent calculation data on empty and filled skutterudites.[15,20,30,40–42]

The characterization of the vibrational dynamics of a material by a set of normal modes exerts strong constraints on models accounting for the material heat-transport properties. On the level of microscopic dynamics, any interaction between vibrational eigenstates which is, apart from finite-size effects, scattering at defects, and boundaries in crystals, the origin of finite phonon lifetime, and hence of finite thermal conductivity, has to follow strictly the rules of energy and momentum conservation. A perturbation of heat transport and hence of thermal conductivity upon respecting those conservation laws can be accounted for by the contribution of lattice vectors $\vec{G}_{\mathrm{hkl}}$ to a multiphonon scattering process, which is known as umklapp scattering.[3,24,25,33,43] Umklapp scattering is not an exclusive property of materials whose vibrational dynamics can be approximated by the Debye model. Due to the hybridization of acoustic and Yb-dominated low-energy optic modes, the Debye model is indeed an insufficient approximation to the low-energy dynamics of $YbFe_4Sb_{12}$. So, likely, parameters derived with this model such as the bare Debye temperature and bare Debye frequency have a reduced importance for characterizing the low-energy dynamics and associated transport properties of $YbFe_4Sb_{12}$.[44] We may expand this conjecture to the dynamics of $LaFe_4Sb_{12}$ and likely to some other filled skutterudite structures.[5,20,31,32,45,46]

A fingerprint of enhanced multiphonon events can be viewed in the departure of the inelastic response from a harmonic behavior. Here, we have probed the temperature dependence as it has been discussed recently for basic anharmonic models.[7,8,11] For the sake of convienence, Fig. 12 displays the experimentally derived energy dependence of the two Yb-dominated peaks with the characteristic energy E^* and $T^* = E^*/k_B$ of the peaks averaged over data taken at $T \lesssim 100$ K.

Qualitatively, some properties of and changes in the low-energy inelastic response of $YbFe_4Sb_{12}$ upon heating are captured by the anharmonic models. For example, the phonon dispersion in the model of Yamakage *et al.* (see Ref. 8) is reminiscent of a symmetry-avoided anticrossing characteristic. A blue shift of modes with increasing T is derived from all those models. Indeed, when applying the isotropic single-particle model of Dahm and Ueda (see Ref. 7) we find a correspondence with experimental as well as DFT-calculated results. From the experimental data of the high-energy peak at $T \gtrsim 100$ K, we obtain for a particle with the mass of Yb M_{Yb} a very small anharmonicity parameter

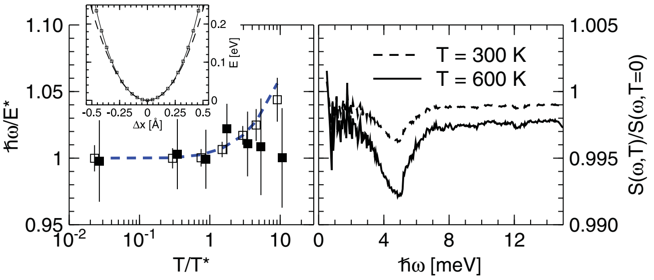

FIG. 12. (Color online) Left, scaled mode energy of the two prominent peaks. Full and empty squares represent peaks with $E^* = 4.8$ and 5.7 meV, respectively. Blue dashed line indicates the effect of the anharmonic term Bx^4 in the Yb potential derived from DFT calculation. Inset, displays the DFT-calculated Yb potential and dashed and solid lines correspond to fit results with harmonic Ax^2 and anharmonic $Ax^2 + Bx^4$ models, respectively. Right, relative changes in the inelastic intensity due to the temperature dependence of the Debye-Waller factor computed within the harmonic approximation.

$\beta = 4B\hbar^4(M_{\mathrm{Yb}}^2 E^{*3})^{-1} = 0.013 \pm 0.003$. On the other hand, a $\beta' = 0.014$ is derived by fitting the potential of Yb calculated from DFT as presented in the inset of Fig. 12 (see also Fig. 3 of Ref. 6) with the anharmonic model $f(x) = Ax^2 + Bx^4$ ($A = 0.88\,\mathrm{eV/Å^2}$, $B = 1.16\,\mathrm{eV/Å^4}$, and fit range $[-0.25 : 0.25]$ Å). The resulting $\hbar\omega/E^*$ behavior is indicated by the blue dashed line in Fig. 12. Consequently, within the single-particle model, the anharmonicity approximated from the INS data is of the order of the quartic term of the DFT-based Yb potential.

The three-dimensional anharmonic oscillator model of Hattori and Tsunetsugu (see Ref. 11) anticipates, even in the case of a purely quartic anharmonic potential, a renormalization of the phonon density of states. It is in accordance not only with a blue shift but also with a spread of excitations resulting in an apparent intensity decrease and mode broadening toward higher T as it has been conjectured from the experimental data at $T \approx 600$ K. We may rule out that the T dependence of the Debye-Waller factor calculated within the harmonic approximation is the origin for the intensity drop-off since the calculated relative intensity changes as displayed in Fig. 12 are one order of magnitude smaller than the experimentally derived values.

There are, as well, deviations of the modelled from measured data, highlighting the enhanced complexity of the lattice dynamics of the real materials. For example, we might conjecture from the model of Yamakage *et al.* the energy of both Yb-dominated peaks to scale with T in a similar way. This is apparently not the case in the experiment. Another departure concerns the temperature dependence of modes above the prominent double peak, which are expected to show a blue shift upon heating, yet smaller than the shift of the double peak. The experimental data give evidence of a red shift of all peaks apart from the Yb-dominated double peak.

Finally, we wish to highlight that the data quality and interpretation depends on experimental constraints. There are constraints that one cannot overcome, such as the scattering power $\propto Z^2$ in comparison to absorption effects $\propto Z^4$ in IXS experiments, leading to the weak signal in our experiment. Others, such as the energy resolution of the spectrometers, e.g., $\Delta E \approx 200$ μeV at about 5 meV at IN6@ILL, might be surpassed in future and a more detailed and accurate characterization of the dynamics of polycrystalline materials could be made possible, e.g., going beyond the approximation of the Yb-dominated modes by a double peak. Nonetheless, the present performance of angle-dispersive IXS and INS spectrometers with the aid of dedicated simulation tools allows one to give a more detailed picture of the cation dynamics of Ca-, Sr-, Ba-, and Yb-filled $\mathrm{Fe_4Sb_{12}}$ than in terms of rattling Einstein modes. The phonon dynamics of completely filled iron antimonides studied here is the dynamics of crystals, not of glasses.

However, owing to the necessity of studying polycrystalline materials, a comprehensive treatment and interpretation of anharmonic effects is made difficult on the basis of the powder-averaged signal. The reference to the basic anharmonic models is established in this paper as an implication of this difficulty. A more rigorous theoretical description of anharmonicity of crystalline matter and its consequences for scattering experiments is well established (e.g., see Ref. 47 and references therein). Its experimental verification requires the monitoring of the dynamic structure factor $S(\vec{Q},\omega,T)$ in the five-dimensional parameter space of momentum $\vec{Q}$, energy $\hbar\omega$, and temperature T.

V. SUMMARY

We have studied the angle-dispersive inelastic response of polycrystalline $M\mathrm{Fe_4Sb_{12}}$ (with $M =$ Ca, Sr, Ba, and Yb) by neutron and x-ray scattering techniques and powder average lattice dynamics calculations. The experimental, coherent signal, revealing the collective dynamics of the compounds, can be well accounted for by the lattice-dynamics calculations and, hence, a set of normal modes. An appreciable localization of eigenmodes and the presence of an extended symmetry-avoided anticrossing phonon dispersion at low energies in $\mathrm{YbFe_4Sb_{12}}$ has been established by the experiments and reproduced by the calculations.

Temperature-dependent measurements have revealed a global softening of the vibrational properties upon heating, consistent with the quasi harmonic approximation. In $\mathrm{YbFe_4Sb_{12}}$ a weak but measurable hardening of ytterbium-dominated eigenstates at about 5.7 meV is established at elevated temperatures. This hardening is of relevance to the temperature response of recently introduced anharmonic lattice-dynamics models. No such peculiar anharmonic effects are observed in the alkaline-earth-filled iron antimonides in the energy range of low-frequency heat-carrying acoustic phonons.

From powder-average-lattice-dynamics calculations the velocity of sound, Debye temperature, and elastic constants have been derived for the compounds $M\mathrm{Fe_4Sb_{12}}$ ($M =$ Ca, Sr, Ba, and Yb). These values are in good agreement with experimental data from literature as far as available. The dependence of the material properties upon the filler cations should motivate further experimental studies of material properties.

ACKNOWLEDGMENTS

Efim Katz and Helmut Schober are thanked for helpful discussions. M.M.K. acknowledges the access to ILL's "Scientific Computing" facility.

---

[1] G. P. Meisner, D. T. Morelli, S. Hu, J. Yang, and C. Uher, Phys. Rev. Lett. **80**, 3551 (1998).

[2] D. M. Rowe, *CRC Handbook of Thermoelectrics* (CRC Boca Raton, 1995).

[3] G. S. Nolas, J. Sharp, and H. J. Goldsmid, *Thermoelectrics Basic Principles and New Materials Developments* (Springer, 2001).

[4] G. J. Snyder and E. S. Toberer, Nat. Mater. **7**, 105 (2008).

[5] M. M. Koza, M. R. Johnson, R. Viennois, H. Mutka, L. Girard, and D. Ravot, Nat. Mater. **7**, 805 (2008).

[6] M. M. Koza, L. Capogna, A. Leithe-Jasper, H. Rosner, W. Schnelle, H. Mutka, M. R. Johnson, C. Ritter, and Y. Grin, Phys. Rev. B **81**, 174302 (2010).

[7] T. Dahm and K. Ueda, Phys. Rev. Lett. **99**, 187003 (2007).

[8] A. Yamakage and Y. Kuramoto, J. Phys. Soc. Jpn. **78**, 064602 (2009).

[9] K. Iwasa, M. Kohgi, H. Sugawara, and H. Sato, Physica B **378-380**, 194 (2006).

[10] K. Iwasa, Y. Mori, L. Hao, Y. Murakami, M. Kohgi, H. Sugawara, and H. Sato, J. Phys.: Conf. Ser. **92**, 012122 (2007).

[11] K. Hattori and H. Tsunetsugu, Phys. Rev. B **81**, 134503 (2010).

[12] H. Mutka, M. M. Koza, M. R. Johnson, Z. Hiroi, J.-I. Yamaura, and Y. Nagao, Phys. Rev. B **78**, 104307 (2008).

[13] N. Bernstein, J. L. Feldman, and D. J. Singh, Phys. Rev. B **81**, 134301 (2010).

[14] Note that at the early stages of research of $YbFe_4Sb_{12}$, the role of itinerant mangetism of the Fe-Sb host structure was not fully explored, resulting in an inadequate attribution of magnetic properties to the Yb-valence state, carried out, as well, by one of the authors of this study.[48] Meanwhile, extensive experimental as well as theoretical studies (see Refs. 49 and 50) have shown that Yb is unambigiously divalent in $YbFe_4Sb_{12}$.

[15] D. Wee, B. Kozinsky, N. Marzari, and M. Fornari, Phys. Rev. B **81**, 045204 (2010).

[16] W. Schnelle, A. Leithe-Jasper, H. Rosner, R. Cardoso-Gil, R. Gumeniuk, D. Trots, J. A. Mydosh, and Y. Grin, Phys. Rev. B **77**, 094421 (2008).

[17] A. Leithe-Jasper, W. Schnelle, H. Rosner, R. Cardoso-Gil, M. Baenitz, J. A. Mydosh, Y. Grin, M. Reissner, and W. Steiner, Phys. Rev. B **77**, 064412 (2008).

[18] E. Burkel, Rep. Prog. Phys. **63**, 171 (2000).

[19] F. Sette and M. Krisch, in *Neutron and X-Ray Spectroscopy*, edited by F. Hippert, E. Geissler, J. L. Hodeau, E. Lelièvre-Berna, and J. R. Regnard (Springer, 2006), pp. 169–188.

[20] J. L. Feldman, P. Dai, T. Enck, B. C. Sales, D. Mandrus, and D. J. Singh, Phys. Rev. B **73**, 014306 (2006).

[21] G. J. Long, R. P. Hermann, F. Grandjean, E. E. Alp, W. Sturhahn, C. E. Johnson, D. E. Brown, O. Leupold, and R. Ruffer, Phys. Rev. B **71**, 140302(R) (2005).

[22] H.-C. Wille, R. P. Hermann, I. Sergueev, O. Leupold, P. van der Linden, B. C. Sales, F. Grandjean, G. J. Long, R. Ruffer, and Y. V. Shvyd'ko, Phys. Rev. B **76**, 140301 (2007).

[23] V. F. Sears, Neutron News **3**, 26 (1992).

[24] S. Lovesey, *Theory of Neutron Scattering from Condensed Matter* (Oxford Science, Oxford, UK, 1984).

[25] G. Squires, *Introduction to the Theory of Thermal Neutron Scattering* (Dover, New York, 1996).

[26] H. Mutka, *Focusing Bragg Optics* (Elsevier Science, North Holland, 1994), pp. 144–150.

[27] M. M. Koza, Phys. Rev. B **78**, 064303 (2008).

[28] χ^2 minimization method is applied with function $f(x) = a + bx + c\exp(-dx) + \sum_{i=1}^{2} A_i \exp\frac{-(x-E_i)^2}{2\sigma_i^2}$. Fit to $G(\omega)/\omega^2$: $b = 0$ throughout and a determined as average value from IN6@ILL data at 300 and 600 K for $1 \leqslant \hbar\omega \leqslant 2.5$ meV and fixed for all fits. Coefficients c and d fitted exclusively to IN4@ILL data for $1 \leqslant \hbar\omega \leqslant 2.5$ meV and fixed for the fit of the Gaussian part. Gaussian parameters A_i, E_i, and σ_i fitted in the energy range 3.5–6.5 meV. Fit to $S(Q,\omega)$: $c = 0$ throughout, a and b approximate the background at $2 \leqslant \hbar\omega \leqslant 8$ meV. Gaussian parameters A_i, E_i, and σ_i fitted in the energy range 3.5–6.5 meV.

[29] J. L. Feldman and D. J. Singh, Phys. Rev. B **53**, 6273 (1996).

[30] M. Rotter, P. Rogl, A. Grytsiv, W. Wolf, M. Krisch, and A. Mirone, Phys. Rev. B **77**, 144301 (2008).

[31] J. L. Feldman, D. J. Singh, I. I. Mazin, D. Mandrus, and B. C. Sales, Phys. Rev. B **61**, R9209 (2000).

[32] J. L. Feldman, D. J. Singh, C. Kendziora, D. Mandrus, and B. C. Sales, Phys. Rev. B **68**, 094301 (2003).

[33] N. Ashcroft and N. Mermin, *Solid State Physics* (Saunders College Philadelphia, USA, 1976).

[34] T. Caillat, A. Borshchevsky, and J. P. Fleurial, J. Appl. Phys. **80**, 4442 (1996).

[35] D. Mandrus, B. C. Sales, V. Keppens, B. C. Chakoumakos, P. Dai, L. A. Boatner, R. K. Williams, T. W. Darling, A. Migliori, M. B. Maple, D. A. Gajewski, and E. J. Freeman, *Thermoelectric Materials—New Directions and Approaches, MRS Symposia Proceedings* (Materials Research Society, Pittsburgh, PA, 1997), Vol. 478, pp. 199–209.

[36] B. C. Sales, D. Mandrus, B. C. Chakoumakos, V. Keppens, and J. R. Thompson, Phys. Rev. B **56**, 15081 (1997).

[37] C. Recknagel, N. Reinfried, P. Hohn, W. Schnelle, H. Rosner, Y. Grin, and A. Leithe-Jasper, Sci. Technol. Adv. Mater. **8**, 357 (2007).

[38] L. Zhang, G. Rogl, A. Grytsiv, S. Puchegger, J. Koppensteiner, F. Spieckermann, H. Kabelka, M. Reinecker, P. Rogl, W. Schranz, M. Zehetbauer, and M. A. Carpenter, Mater. Sci. Eng. B **170**, 26 (2010).

[39] J. Hafner, J. Comput. Chem. **29**, 2044 (2008).

[40] P. Ghosez and M. Veithen, J. Phys. Condens. Matter **19**, 096002 (2007).

[41] A. L. Martinotto, V. Gava, and C. A. Perottoni, Phys. Rev. B **81**, 104112 (2010).

[42] I. K. Dimitrov, M. E. Manley, S. M. Shapiro, J. Yang, W. Zhang, L. D. Chen, Q. Jie, G. Ehlers, A. Podlesnyak, J. Camacho, and Q. Li, Phys. Rev. B **82**, 174301 (2010).

[43] V. Murashov and M. A. White, *Thermal Conductivity: Theory, Properties, and Applications*, edited by T. Tritt (Kluwer Academic/Plenum Publishers, New York, 2004), pp. 93–104.

[44] G. A. Slack, Phys. Rev. B **22**, 3065 (1980).

[45] C. Lee, I. Hase, H. Sugawara, H. Yoshizawa, and H. Sato, J. Phys. Soc. Jpn. **75**, 123602 (2006).

[46] S. Tsutsui, H. Kobayashi, D. Ishikawa, J. P. Sutter, A. Q. R. Baron, T. Hasegawa, N. Ogita, M. Udagawa, Y. Yoda, H. Onodera, D. Kikuchi, H. Sugawara, C. Sekine, I. Shirotani, and H. Sato, J. Phys. Soc. Jpn. **77**, 033601 (2008).

[47] R. A. Cowley, Rep. Prog. Phys. **31**, 123 (1968).

[48] A. Leithe-Jasper, D. Kaczorowski, P. Rogla, J. Bogner, M. Reissner, W. Steiner, G. Wiesinger, and C. Godart, Solid State Commun. **109**, 395 (1999).

[49] W. Schnelle, A. Leithe-Jasper, M. Schmidt, H. Rosner, H. Borrmann, U. Burkhardt, J. A. Mydosh, and Y. Grin, Phys. Rev. B **72**, 20402 (2005).

[50] Y. S. Dedkov, S. L. Molodtsov, H. Rosner, A. Leithe-Jasper, W. Schnelle, M. Schmidt, and Y. Grin, Physica C **460-462**, 698 (2007).